

## Article

# Phase and Microstructure Transition of High Cu Content Cu-W Composite Powder Fabricated by Spray Drying

Qi Wang <sup>1</sup>, Xiuqing Li <sup>2,\*</sup> , Shizhong Wei <sup>2,\*</sup> , Wenpeng Lou <sup>1</sup>, Liujie Xu <sup>2</sup> and Yucheng Zhou <sup>2</sup>

<sup>1</sup> School of Materials Science & Engineering, Henan University of Science and Technology, Luoyang 471023, China

<sup>2</sup> National Joint Engineering Research Center for Abrasion Control and Molding of Metal Materials, Henan University of Science and Technology, Luoyang 471003, China

\* Correspondence: li\_xq@sina.cn (X.L.); wsz@haust.edu.cn (S.W.)

**Abstract:** Cu-W composite powder with various W contents (0, 10, 20, and 30 wt%) has been fabricated by spray drying, calcination, and two-stage hydrogen reduction in this work. The microstructures and phase evolution of Cu-W composite powder were studied by FESEM, HRTEM, and XRD. Results show that precursor powder is composed of  $\text{Cu}_2(\text{OH})_3\text{NO}_3$  and  $\text{H}_2\text{WO}_4 \cdot \text{H}_2\text{O}$ . Spherical  $\text{CuWO}_4$  with a particle size of about 50 nm and micron-scale flat flake CuO were obtained when the calcination temperature was 500 °C. Through chemical vapor transport (CVT) during the reduction process, volatile  $\text{WO}_2(\text{OH})_2$  continuously migrates to the copper surface and is reduced to W, resulting in a W-coated Cu structure. This coating structure can inhibit the aggregation and growth of copper particles. The particle sizes of Cu-10 wt%W, Cu-20 wt%W, and Cu-30 wt%W composite powders are 9.309  $\mu\text{m}$ , 8.440  $\mu\text{m}$ , and 6.290  $\mu\text{m}$ , reduced by 40.51%, 46.06%, and 59.80%, respectively, compared to the particle size of pure copper powder, 15.648  $\mu\text{m}$ . With increasing W content, the W-coated Cu particles gradually become denser and trend to grow from sphere to flake.



**Citation:** Wang, Q.; Li, X.; Wei, S.; Lou, W.; Xu, L.; Zhou, Y. Phase and Microstructure Transition of High Cu Content Cu-W Composite Powder Fabricated by Spray Drying. *Metals* **2022**, *12*, 1522. <https://doi.org/10.3390/met12091522>

Academic Editor:  
Masahiro Fukumoto

Received: 22 August 2022  
Accepted: 12 September 2022  
Published: 15 September 2022

**Publisher's Note:** MDPI stays neutral with regard to jurisdictional claims in published maps and institutional affiliations.



**Copyright:** © 2022 by the authors. Licensee MDPI, Basel, Switzerland. This article is an open access article distributed under the terms and conditions of the Creative Commons Attribution (CC BY) license (<https://creativecommons.org/licenses/by/4.0/>).

**Keywords:** high Cu content; spray drying; phase evolution; hydrogen reduction

## 1. Introduction

Cu possesses remarkable electrical and thermal conductivity, while W has high hardness, high strength, and low thermal expansion coefficient. Based on maintaining the copper's advantages, the existence of the tungsten phase significantly improves the strength, wear resistance, and arc resistance of Cu-W composites with high Cu content, making it widely used as electrodes and electrical contacts. The W(70–90) wt%-Cu alloy has high thermal conductivity and low coefficient of thermal expansion, making it an ideal packaging material for electronic devices. It is, therefore, widely used in integrated circuits and electronic devices [1–5].

Because of the great difference in melting point and insolubility of W and Cu, the powder metallurgy method is normally used to prepare Cu-W composites. Melting-infiltration is the traditional method, which is limited to Cu-W composites with low Cu content and results in product inhomogeneity due to uneven porosity in preforms [6]. Adding a small amount of sintering agent into Cu-W composites, such as Co, Ni, or Fe, the density can be increased, but their electrical and thermal conductivity would deteriorate [7]. For the Cu-W system, particle rearrangement is the dominant mechanism for sintering densification; fine particles with uniform size and composition can help improve the sintering performance of the composite powder and facilitate the preparation of high-performance Cu-W composites [8,9]. Homogeneous and ultrafine Cu-W composite powders are prepared by the mechanical alloying method [10], hydrothermal synthesis method [11], chemical co-deposition method [12], and spray drying method [13]. Unfortunately, mechanical alloying methods can easily introduce impurity elements such as Fe, Co, and O, which will have a similar deteriorating effect as sintering activators. In addition, foreign elements

would increase as the milling time goes on, resulting in a decrease in relative density [14,15]. Recent studies have shown that the preparation of nanoscale or ultrafine Cu-W composite powder through chemical precipitation, calcination, and hydrogen reduction can effectively avoid contamination [16,17].

W-20 wt%Cu composite powder has been prepared by Hong et al. [18] through a mechanical thermochemical process. The size of the W particle was about 30–100 nm, and its composition distribution was uniform. The W-20 wt%Cu composite had high purity and high density. In particular, it has close to theoretical thermal conductivity. Hong et al. [19] also prepared W-(10~40) wt%Cu nanocomposite powders through calcination and subsequent reduction in spray-dried Cu-W salts. After sintering at 1250 °C for 1 h, the high density was higher than 98%. Fang et al. [20] found that the powder prepared by spray drying has a small particle size and high activity. Spray drying technology also has the characteristics of a simple operation, high efficiency, and short cycle time. Therefore, the method is expected to achieve industrial production and has a promising application.

There is currently more research on preparing Cu-W composite powders with a high level of tungsten, but few studies on preparing Cu-W composite powders with a high level of copper. Cu-30 wt%W nanocomposite powders were produced by Wang et al. [21] with a method of chemical coprecipitation. However, there are few systematic studies on the phase and microstructure transition in the preparation of high-copper-content Cu-W composite powders during the spray drying process. Thus, ultrafine Cu-W composite powders with various tungsten contents (0, 10, 20, and 30 wt%) have been produced through spray drying, and hydrogen reduction. A detailed investigation of the synthesis mechanism, phase transformation, and microstructure at different stages has been carried out. Additionally, the effects of calculation temperature and tungsten content on the powders' morphology and phase composition have also been analyzed.

## 2. Materials and Methods

The raw materials for synthesizing Cu-W composite powders are  $(\text{NH}_4)_6\text{H}_2\text{W}_{12}\text{O}_{40}\cdot 4\text{H}_2\text{O}$  (AMT) with a purity of 99%,  $\text{Cu}(\text{NO}_3)_2\cdot 3\text{H}_2\text{O}$  with a purity of 99%, and distilled water. Table 1 gives the synthesized powder-specific composition. The Cu-W composite powder preparation process is presented in Figure 1. The raw materials were dissolved according to the ratio in Table 1, stirred to obtain a homogeneous mixing solution, and then fed into a pressure atomizer. To obtain precursor powders, the atomization rate is 20 mL/min, and the atomized air temperature is 250~300 °C. Cu-W composite powders were obtained after calcining and the process of hydrogen reduction.

**Table 1.** Composition of the synthesized Cu-W composite powders.

W (wt%)	$(\text{NH}_4)_6\text{H}_2\text{W}_{12}\text{O}_{40}\cdot 4\text{H}_2\text{O}$ (AMT) (g)	$\text{Cu}(\text{NO}_3)_2\cdot 3\text{H}_2\text{O}$ (g)	Distilled Water (mL)
0	0	380.13	1000
10	13.93	342.11	1000
20	27.86	304.10	1000
30	41.80	266.09	1000

Phase compositions of the powders obtained during spray drying, calcination, and hydrogen reduction were analyzed using X-ray diffraction (XRD, Bruker D8, Bruker, Karlsruhe, German) with Cu K $\alpha$  radiation ( $\lambda = 1.5406 \text{ \AA}$ ) in the  $2\theta$  range of 10–90°, respectively. Differential scanning calorimeter (DSC, Netzsch, Selb, Germany) and thermogravimetry (TG) were used to analyze the heat absorption and mass change of the precursors. The valence states of the pure copper and Cu-20 wt%W calcined powders were analyzed by XPS. The morphology and chemical composition of the powders were researched with FESEM (JSM-IT800 SHL, JEOL, Tokyo, Japan) and EDS (JEOL, Tokyo, Japan). Moreover, the microstructure of precursor powder was studied with HRTEM (JEM-2100F, JEOL, Tokyo,

Japan). The size distribution was measured by a laser particle sizer (OMCC LS-909, Omecc, Zhuhai, China).

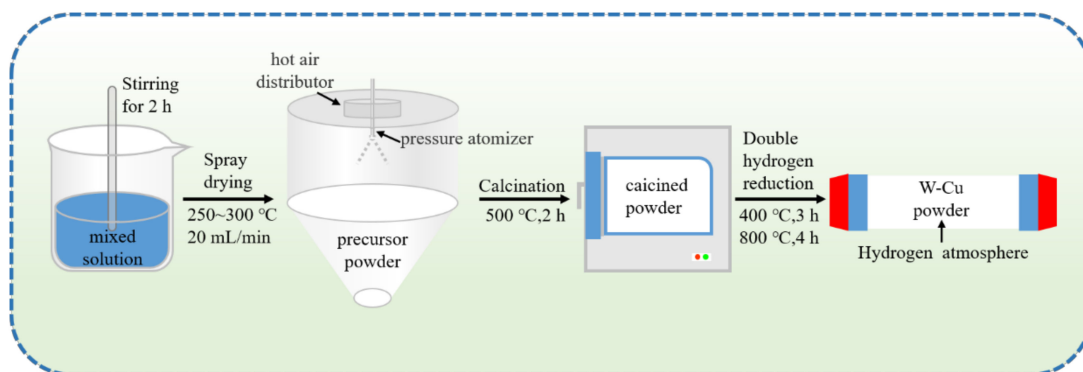
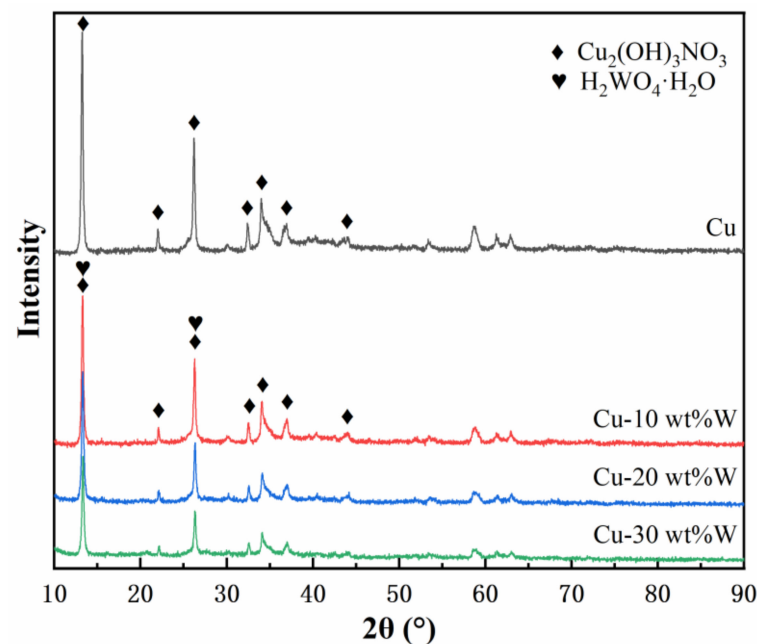


**Figure 1.** The preparing process of Cu-W composite powders.

### 3. Results and Discussion

#### 3.1. Characterization of the Precursor Powders

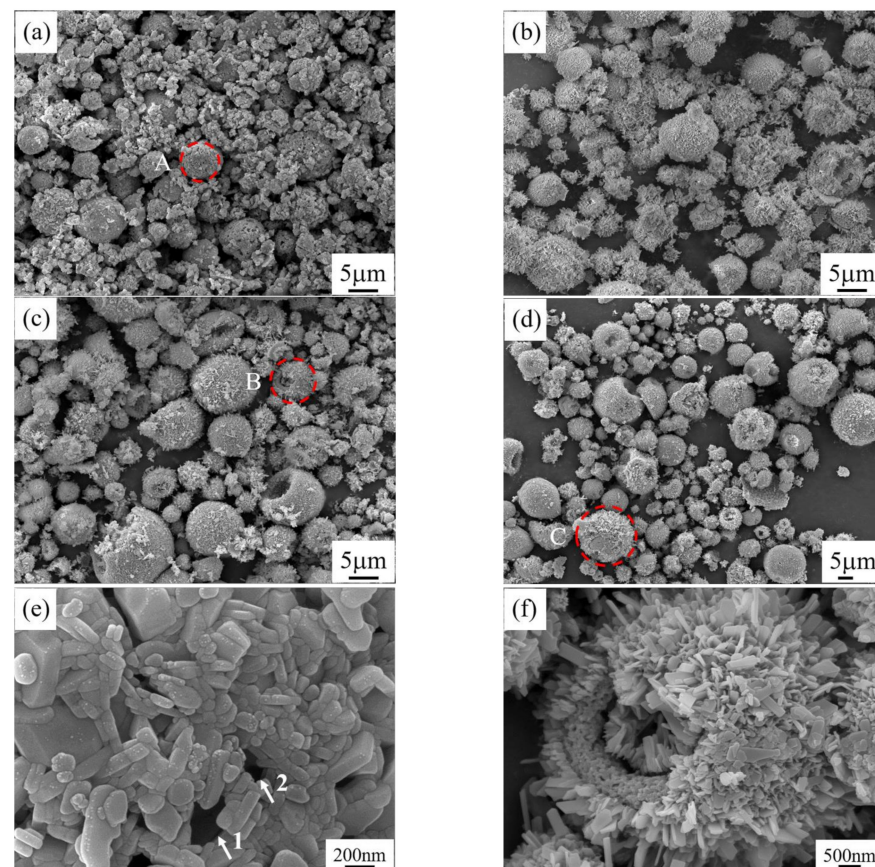
Figure 2 gives the XRD patterns of precursor powders. Pure copper precursor powders consist of  $\text{Cu}_2(\text{OH})_3\text{NO}_3$  (PDF#15-0014), while Cu-W precursor powders consist of  $\text{Cu}_2(\text{OH})_3\text{NO}_3$  and  $\text{H}_2\text{WO}_4 \cdot \text{H}_2\text{O}$  (PDF#18-1420), which can be seen from Figure 2. The intense and narrow peak indicates the high crystallinity of precursor powders.



**Figure 2.** XRD patterns of precursor powders.

SEM images of precursor powders are shown in Figure 3. The precursors are mainly composed of hollow spherical shell-like spheres in a size range of about 5–10  $\mu\text{m}$ , as shown in Figure 3a–d. It can be seen from Figure 3e (a larger version of area A in Figure 3a) that the spherical shells in the pure copper precursor powders are agglomerated by nano-slat structures, and there are obvious holes on the surface of the spherical shells as marked by arrows 1–2. Combined with Figure 2, it can be seen that  $\text{Cu}_2(\text{OH})_3\text{NO}_3$  in the pure copper precursor powders exists in a slatted structure. In contrast, the spherical shells in the Cu-W precursor powders are composed of a large number of nanoscale metal salt particles and nano-slat structures with a radioactive distribution that grows attached to the surface and inside of the spherical shells (Figure 3f). The reason why metal salt particles

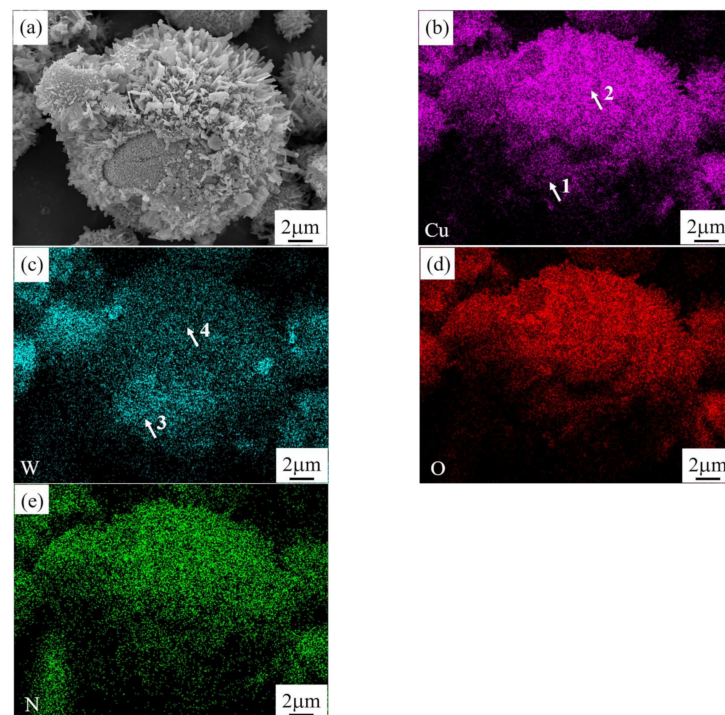
form hollow spherical shells in the spray drying process is that the solution is atomized into mist (actually fine droplets) by a pressure atomizer. The surface of these fine droplets is partially dried rapidly, and the metal salts on the surface precipitate to form a shell layer. The solution inside the droplets continued to evaporate and dry. The precipitated metal salts are adsorbed on the inner surface of the shell layer to make the shell layer thicken continuously. During the evaporation of the inner solution, a large pressure is generated inside the shell to break the shell layer and form spherical shell fragments [22].



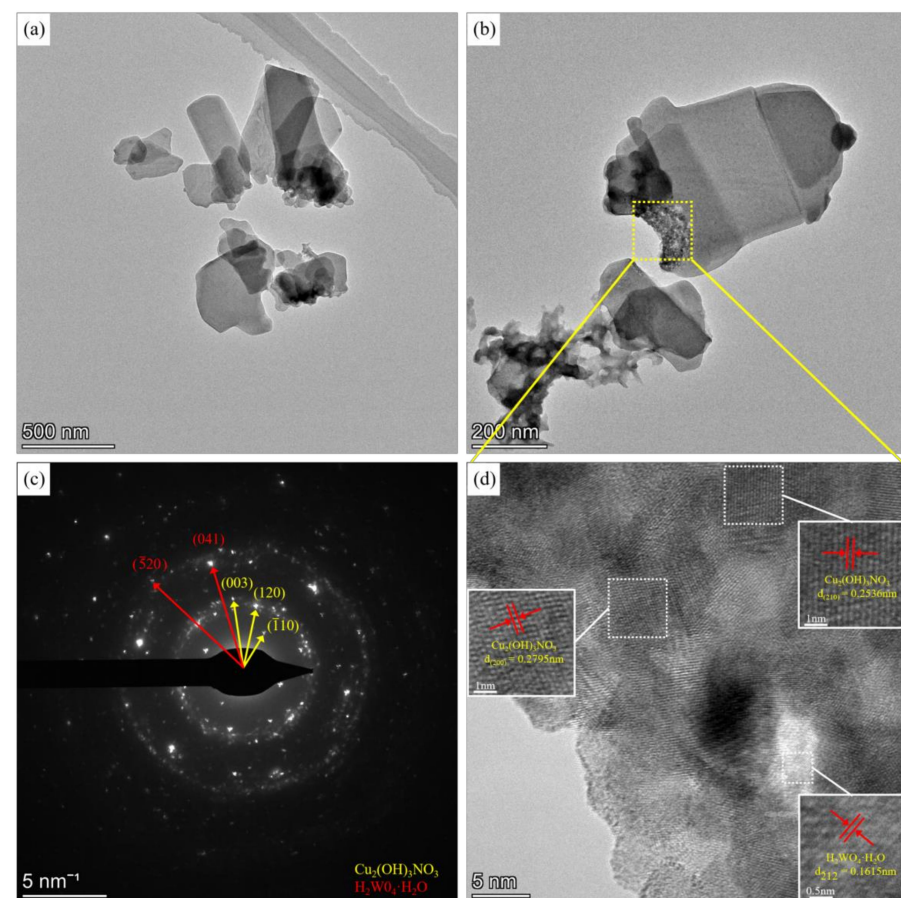
**Figure 3.** SEM images of precursor powders: (a) pure copper precursor powder; (b) Cu-10 wt%W precursor powder; (c) Cu-20 wt%W precursor powder; (d) Cu-30 wt%W precursor powder; (e) the larger version of area A in Figure 3a; (f) the larger version of area B in Figure 3c.

Figure 4 gives the EDS analysis of area C in Figure 3d. The content of Cu on the shell layer is lower than that of the surface slat structure, while the W content is higher than that of the surface slat structure, as marked by arrows 1–4. It is further demonstrated that these slatted structural components are dominantly  $\text{Cu}_2(\text{OH})_3\text{NO}_3$ . Yoon et al. [23] also discovered that the core and surface of the spherical shell have a much higher Cu content than that of the center region.

To further prove the phase structure, TEM micrographs of Cu-20 wt%W precursor powder is provided in Figure 5. The dispersed nano-slat structures can be seen in Figure 5a,b, which are consistent with SEM images in Figure 3f. Figure 5c shows the SAED pattern of the area denoted in Figure 5b, revealing that the two phases are monoclinic phases  $\text{Cu}_2(\text{OH})_3\text{NO}_3$  and  $\text{H}_2\text{WO}_4 \cdot \text{H}_2\text{O}$ . The HRTEM image of the yellow boxed region is given in Figure 5d. The measured lattice stripe spacings are 0.2795 nm, 0.2536 nm, and 0.1615 nm, which approach the spacing of  $\text{Cu}_2(\text{OH})_3\text{NO}_3$  (200), (210), and  $\text{H}_2\text{WO}_4 \cdot \text{H}_2\text{O}$  ( $\bar{2}12$ ) crystal planes of PDF#15-0014 and PDF#18-1420, respectively. All evidence of existence of  $\text{H}_2\text{WO}_4 \cdot \text{H}_2\text{O}$  is consistent with the XRD patterns of precursor powders (Figure 2).

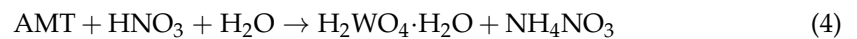
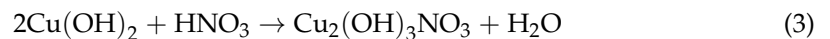


**Figure 4.** EDS distribution diagram of the enlarged view of the region C in Figure 3d: (a) SEM; (b–e) Distribution of element.



**Figure 5.** (a) and (b) TEM images of Cu-20wt%W precursor powders; (c) SAED pattern in the location in Figure 5b; (d) HRTEM image of the medium yellow area in Figure 5b.

$\text{Cu}(\text{NO}_3)_2 \cdot 3\text{H}_2\text{O}$  is readily dissolved to form  $\text{Cu}^{2+}$  and  $\text{NO}_3^-$ , and  $\text{Cu}^{2+}$  hydrolyzes to  $\text{Cu}(\text{OH})_2$  (see reactions 1 and 2).  $\text{Cu}(\text{OH})_2$  and AMT produce  $\text{Cu}_2(\text{OH})_3\text{NO}_3$  and  $\text{H}_2\text{WO}_4 \cdot \text{H}_2\text{O}$  via reactions 3 and 4. The nitric acid required for reactions 3 and 4 is coproduced with  $\text{Cu}(\text{OH})_2$  due to the hydrolysis reaction (see reactions 1 and 2).  $\text{NH}_4\text{NO}_3$  is readily dissolved in water during drying, so the content of  $\text{NH}_4\text{NO}_3$  in the precursors is very little [21,24].

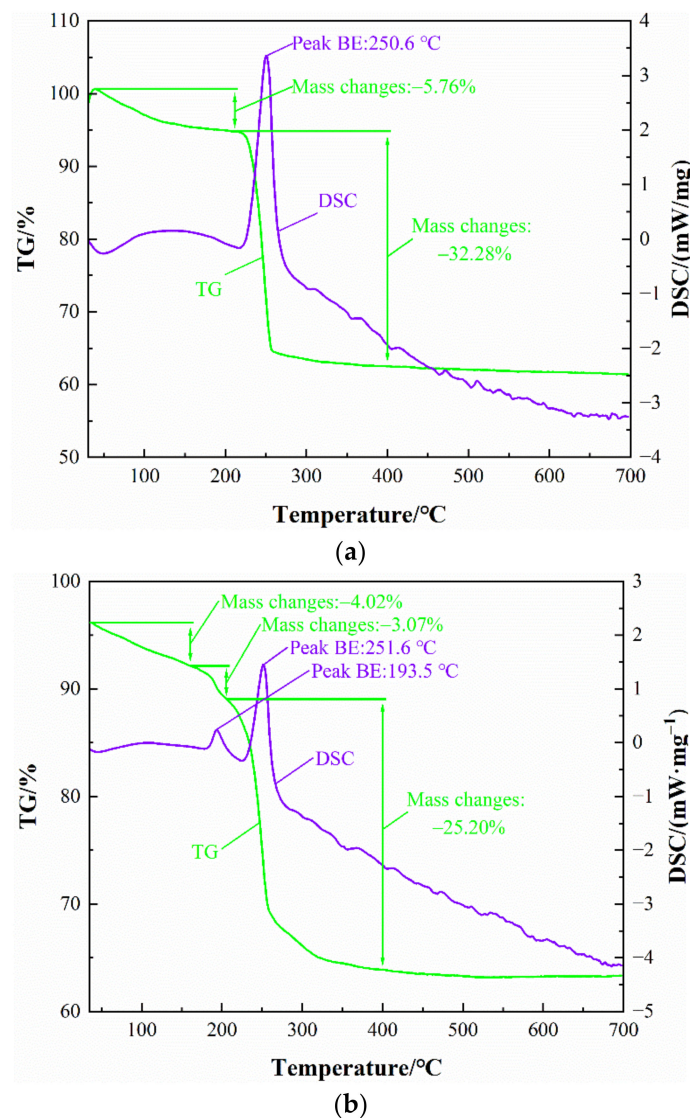


### 3.2. Characterization of the Calcined Powders

To determine the suitable calcination temperature of the precursor powders and ensure a single composition, the fine and uniform particle size of the calcined powders, pure copper, and Cu-20 wt%W precursor powders were selected for TG-DSC analysis from 25 °C to 700 °C. Figure 6 shows the TG-DSC curves of pure Cu and Cu-20 wt%W precursor powders. Pure copper precursor powder on the DSC curve only shows one endothermic peak near 250.6 °C, and the corresponding TG curve shows a sharp decreasing trend between 211.6–400 °C with a mass loss of 32.28% (see Figure 6a), which indicates that  $\text{Cu}_2(\text{OH})_3\text{NO}_3$  decomposes to CuO in this temperature range.

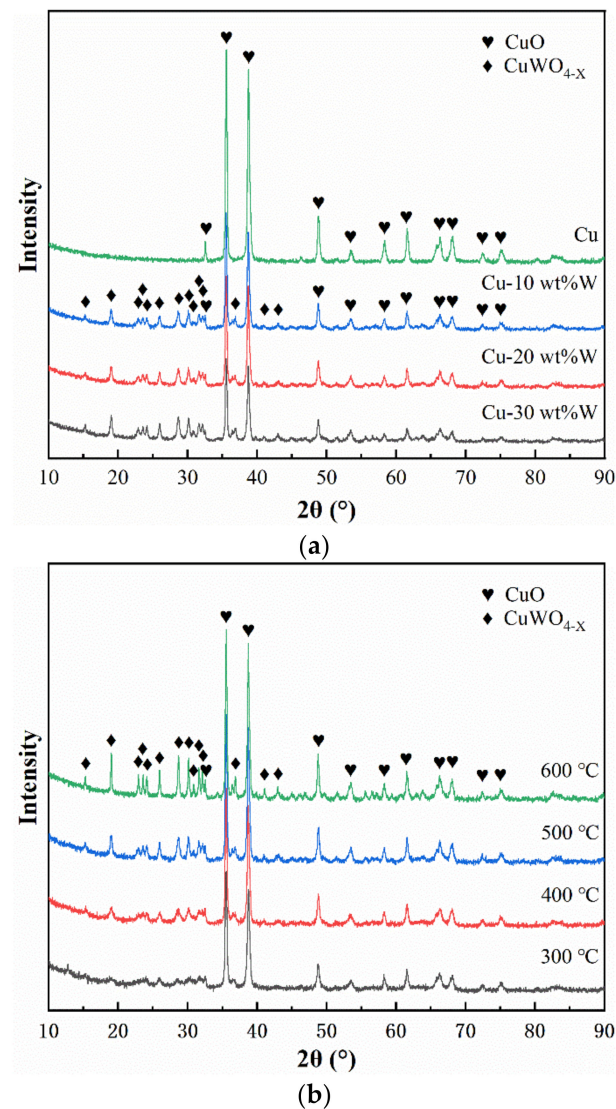
While two endothermic peaks on the DSC curve of Cu-20 wt%W precursor powder are observed in Figure 6b at 160.7–205.6 °C and 205.6–400.4 °C, the weight losses are 3.07% and 25.20%, respectively. The former can be attributed to the removal of crystalline water in  $\text{H}_2\text{WO}_4 \cdot \text{H}_2\text{O}$ , while the latter is related to the transformation of  $\text{Cu}_2(\text{OH})_3\text{NO}_3$  and  $\text{H}_2\text{WO}_4 \cdot \text{H}_2\text{O}$  to Cu-W oxides. TG curves in Figure 6 show little change in weight loss when the temperature is above 500 °C, indicating that the precursor powders were completely decomposed. To investigate the effect of calcination temperature on the powders' morphology and phase composition, the calcination temperature was set as 300–600 °C, and the time was set as 2 h.

Figure 7 gives the XRD patterns of precursor powders with different W content calcined under 500 °C and Cu-20 wt%W precursor powder calcined under different temperatures. Figure 7 reveals that the calcination product of pure Cu precursor powder is CuO, while that of the Cu-W precursor powder is mainly CuO and  $\text{CuWO}_4$ . The diffraction peaks of  $\text{CuWO}_4$  are weak when the precursor powder is calcined at 300 °C (see Figure 7b). As the calcination temperature increases, the content of  $\text{CuWO}_4$  gradually increases, and the diffraction peak becomes higher and sharper.



**Figure 6.** TG and DSC curves of the precursor powders: (a) pure copper precursor powder; (b) Cu-20 wt%W precursor powder.

In order to analyze the valence state of Cu element in pure copper calcined powder and Cu, W element in Cu-W calcined powder, XPS analyses of Cu and Cu-20 wt%W calcined powders under 500 °C were carried out. The binding energies of  $W4f_{7/2}$  and  $W4f_{5/2}$  can fit well with a standard binding energy of  $W^{6+}$  (Figure 8a) [25]. For the O1s peak of pure Cu precursor powder, there are three peaks (Figure 8b): O atoms bound to metals (529.69 eV), defect sites with low O coordination (531.31 eV), and surface  $OH^-$  (532.41 eV) [26]. The O1s peak of the Cu-20 wt%W calcined powder at 530.4 eV can be deconvoluted: 530.1 eV (W-O), 530.6 eV (Cu-O), and 531.6 eV (surface  $OH^-$ ). Figure 8c shows the Cu2p spectra of pure copper and Cu-20 wt%W calcined powders. At 943 eV and 963 eV, two shakeup satellite peaks that are typical for Cu(II) in cupric compounds can be seen [27]. In addition, the binding energies of  $Cu2p_{1/2}$  (954.2 eV) and  $Cu2p_{3/2}$  (934.2 eV) with a 20.0 eV peak spacing were similar to the peak spacing (20.0) of  $Cu2p_{1/2}$  and  $Cu2p_{3/2}$  in the standard CuO spectra. Thus, the calcination products of the pure copper precursor powder are pure CuO, while that of Cu-20 wt%W calcined powder is composed of CuO and  $CuWO_4$ .



**Figure 7.** (a) XRD patterns of precursor powders with different W content calcined under 500 °C for 2 h; (b) XRD patterns of Cu-20 wt%W precursor powders calcined under different temperatures.

SEM images of Cu-20 wt%W calcined powders under different temperatures are shown in Figure 9. At 300 °C, the Cu-20 wt%W calcination powder is composed of broken spherical shells and flocculent powders attached to their surface (Figure 9a). When the calcination temperature rises to 400 °C, the broken spherical shells are transformed into lumpy powders formed by the agglomeration of flattened lamellar particles, and the flocculent powders increase (Figure 9b). Zhu et al. [28] pointed out that, under mild reaction conditions, the aggregation trend of CuO particles may be caused by the low nucleation rate and growth rate of CuO particles. When calcined at 500 °C, the flocculent powders are transformed into fine agglomerated nano-spherical particles and connect dispersed micron-sized flat flake CuO into flakes.

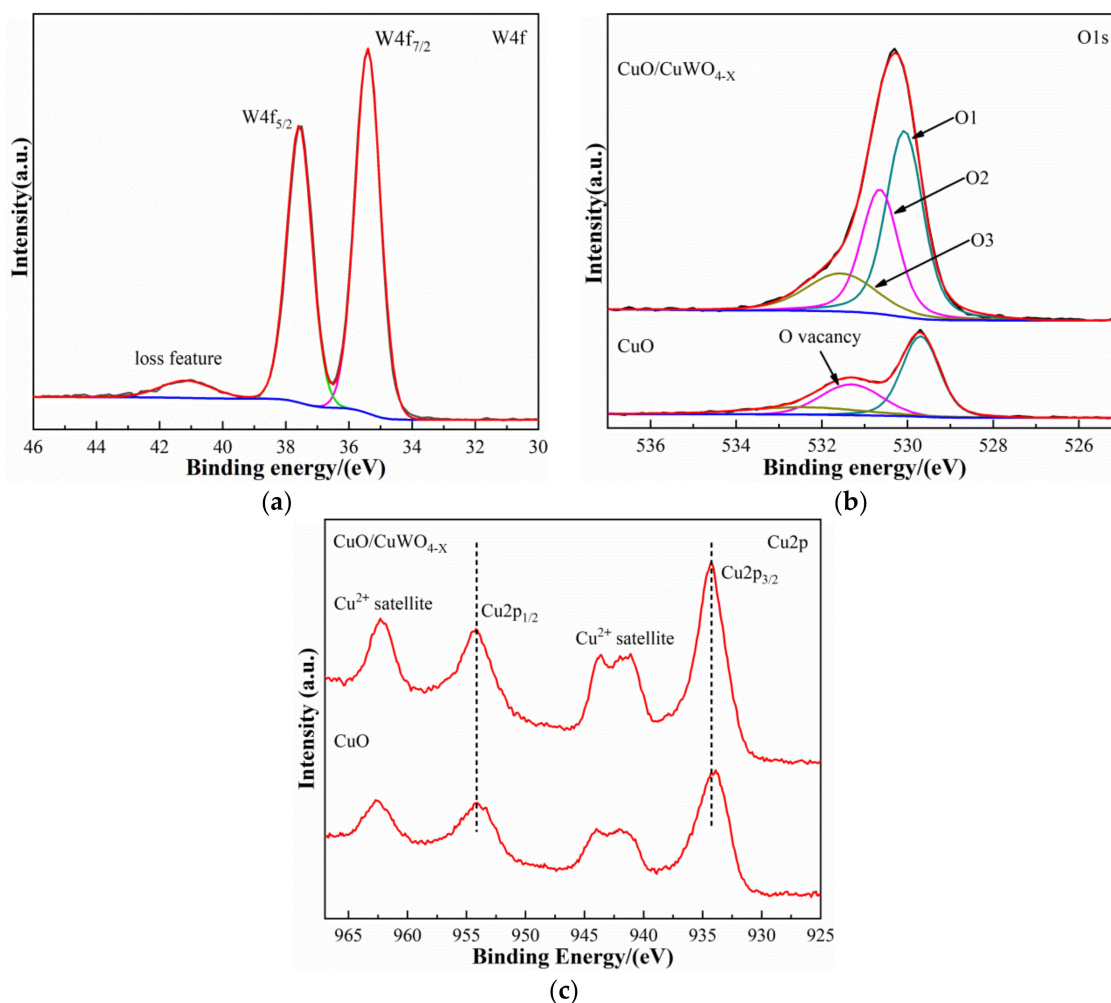


**Figure 8.** XPS spectra of pure Cu and Cu-20 wt%W precursor powders calcined at 500 °C for 2 h: (a) W4f; (b) O1s; (c) Cu2p.

EDS analysis was carried out on the larger version of area A in Figure 9c, and the result is shown in Figure 10. As shown in Figure 10e, the atomic ratio of Cu and O at point A in Figure 10a is close to 1:1, and the atomic ratio of O, Cu, and W at point B in Figure 10a is close to 4: 1:1, which further proves that the flake structure is CuO and the spherical structure is CuWO<sub>4</sub>. This is also consistent with the distribution of elements in Figure 10b–d. Since the calcined powder is nonconductive and needs to be sprayed with gold, the unspecified peaks in Figure 10e,f are Au. However, with the further increase in calcination temperature, these spherical particles easily melt and adhere between the particles, forming large aggregates. The fine particles melt and grow, as shown in Figure 9d in the arrows 1–4 marked particles. Therefore, the optimal calcination temperature of Cu-20 wt%W precursor powder is 500 °C, which is consistent with the analysis in Figure 6b.

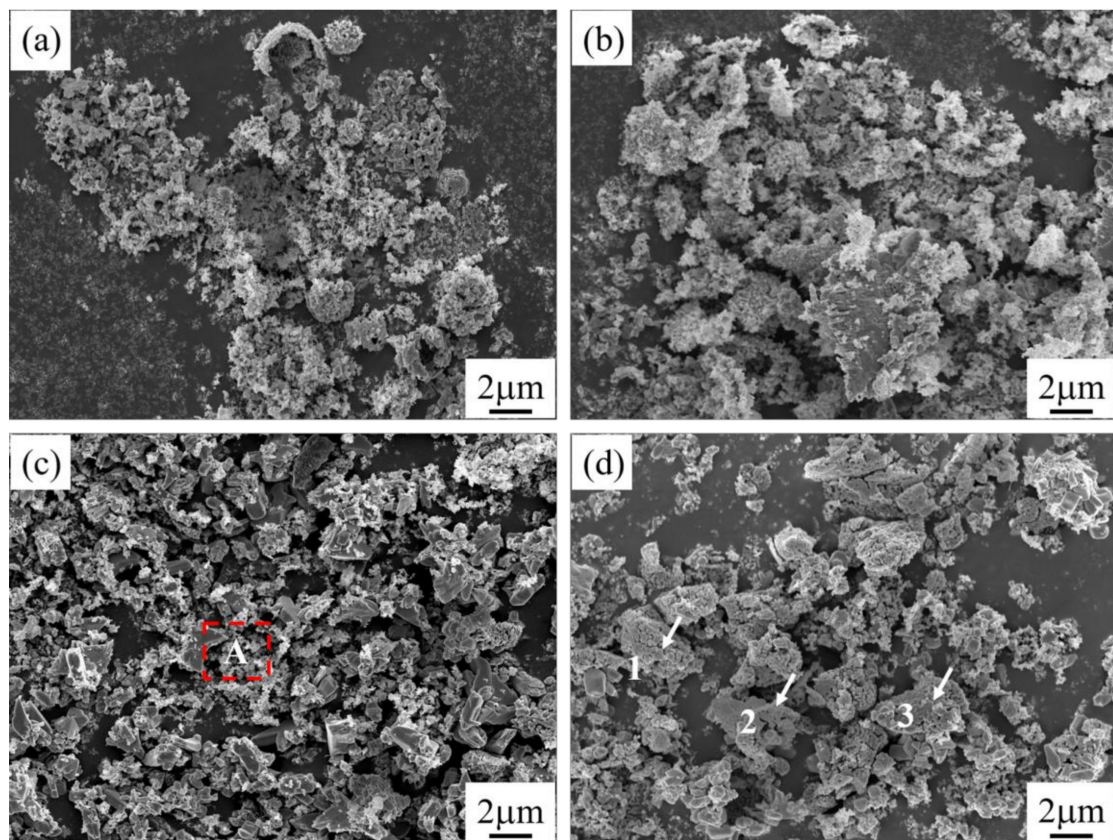


**Figure 9.** SEM images of Cu-20 wt%W precursor powders calcined at different temperature for 2 h: (a) 300 °C; (b) 400 °C; (c) 500 °C; (d) 600 °C.

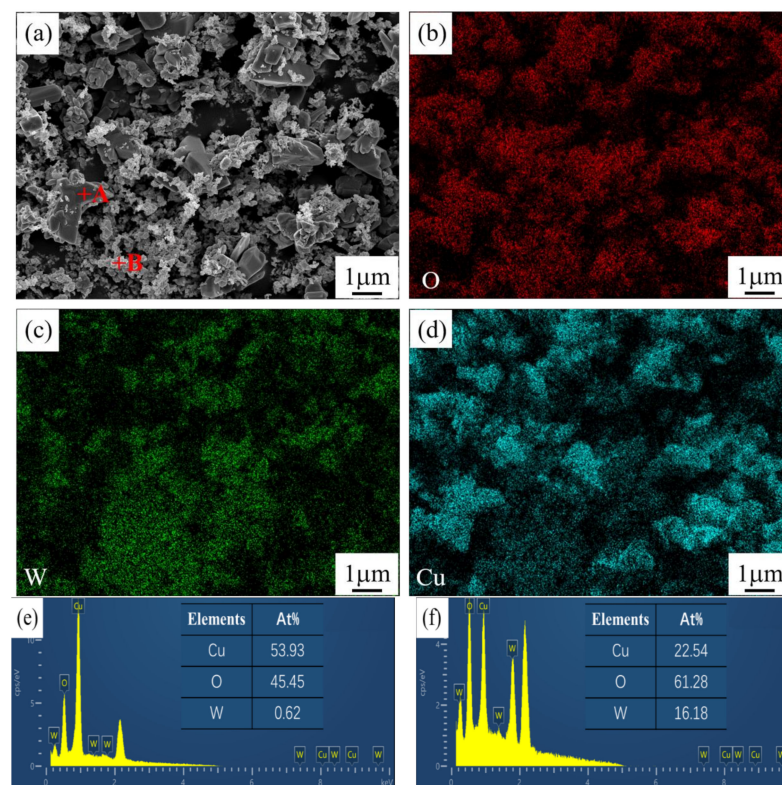


**Figure 10.** EDS distribution diagram of the larger version of area A in Figure 9c: (a) SEM; (b–d) distribution of elements; (e) EDS spectrum of point A; (f) EDS spectrum of point B.

SEM images of pure copper precursor powders calcined at different temperatures are shown in Figure 11. When at low calcination temperatures (Figure 11a,b), the calcined powder size is larger, which are composed of large agglomerates formed by the self-assembly of flake CuO [29]. When the calcination temperature rises to 500 °C, it is clear from the local amplification diagram in Figure 11c that the flake CuO tends to transform into spherical CuO. However, flake CuO is transformed into fine and well-dispersive particles at 600 °C (Figure 11d).

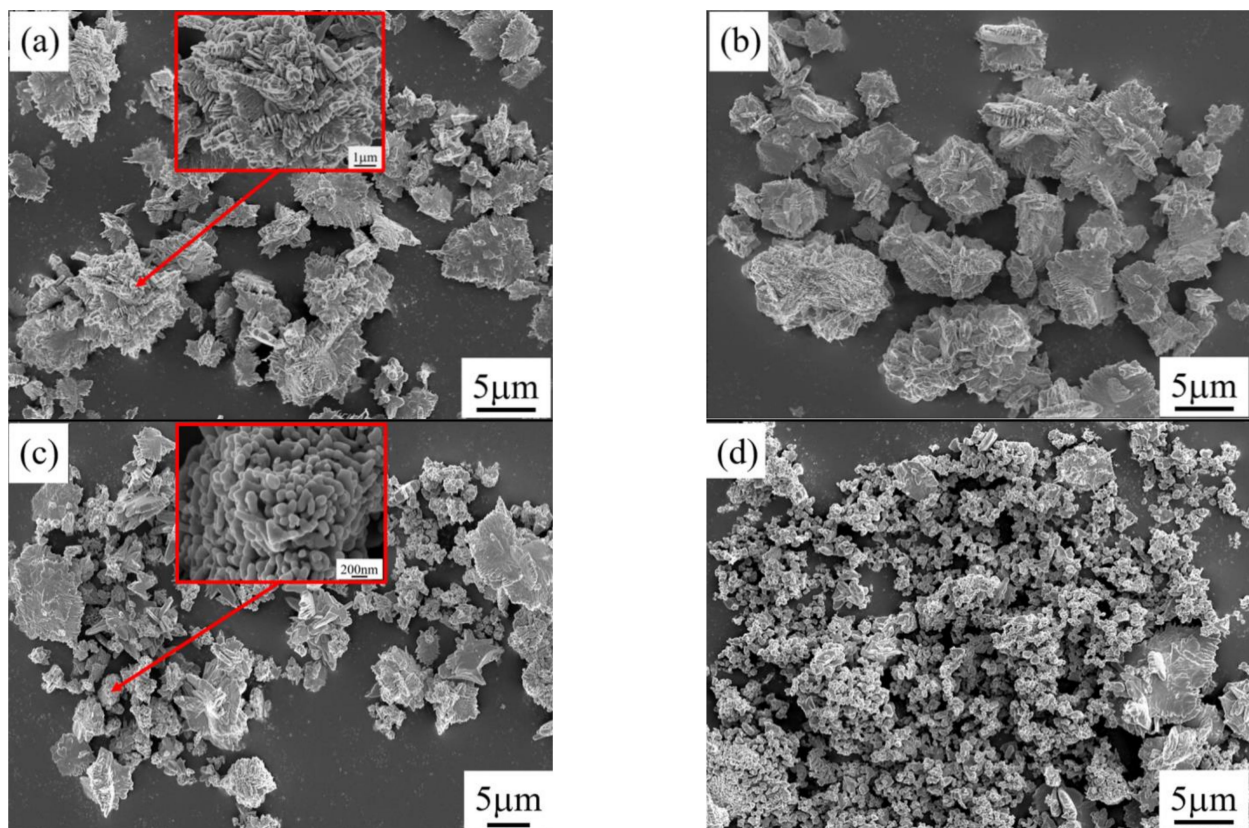


**Figure 11.** SEM images of pure copper precursor powders calcined at different temperature for 2 h: (a) 300 °C; (b) 400 °C; (c) 500 °C; (d) 600 °C.

Cu-10 wt%W and Cu-30wt%W calcined powders at 500 °C and 600 °C for 2 h were observed by SEM, and the results are given in Figure 12. The morphological trends of the Cu-10 wt%W and Cu-20 wt%W calcined powders were similar. When calcined at 500 °C, the agglomerated flat flake CuO particles start to disperse, as shown in arrows 1–2 in Figure 12a, and the flocculent powder is transformed into spherical CuWO<sub>4</sub> particles, the size of which is about 50 nm (Figure 12c). The Cu-30wt%W calcined powder at 500 °C can also be found in the same phenomenon (Figure 12g). The Cu-10 wt%W agglomerated powders begin to disperse at 600 °C (see Figure 12b). An increase in calcination temperature can also cause nano-spherical CuWO<sub>4</sub> particles to grow up and melt (marked by arrows 3 and 4 in Figure 12d). However, Cu-30 wt%W calcined powders at 500 °C and 600 °C retain the hollow spherical shell of the precursor powders (Figure 12e,f), and bulk powders formed by the segregation of CuO and spherical CuWO<sub>4</sub> particles (see Figure 12h). The large aggregate is unfavorable for the subsequent reduction process.

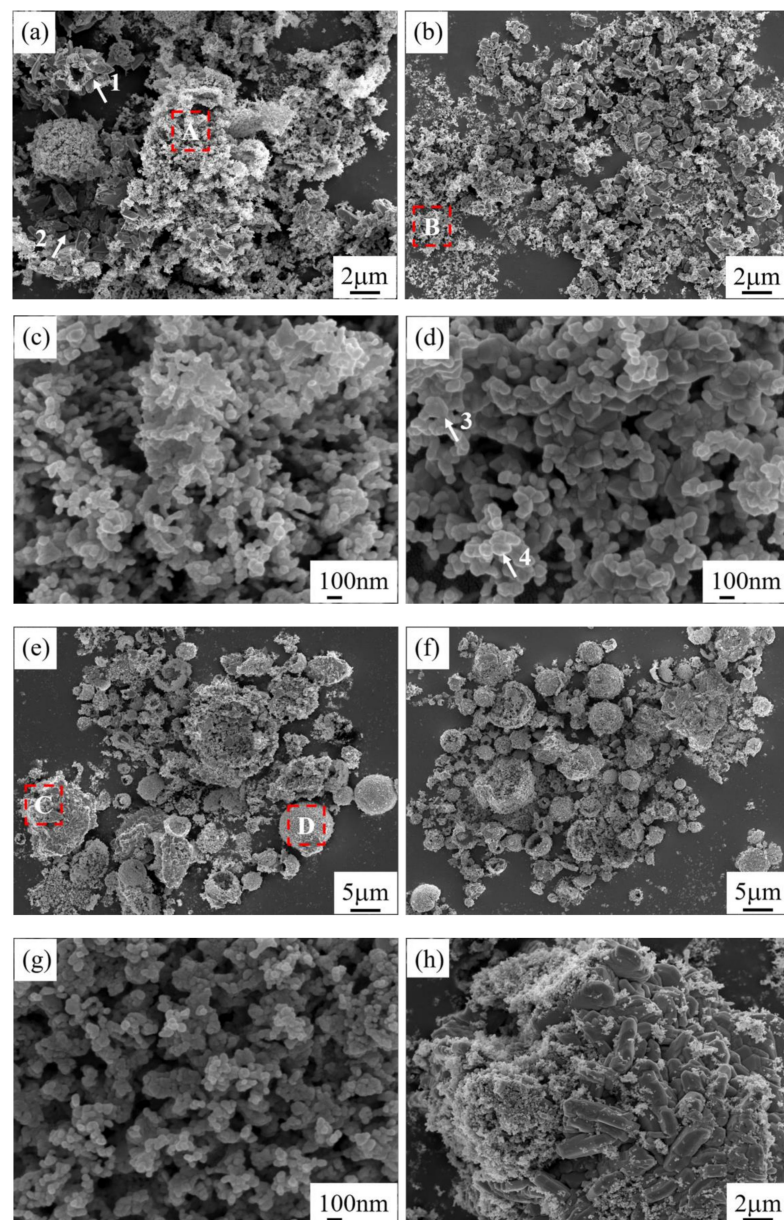


**Figure 12.** SEM images of Cu-10 wt%W and Cu-30 wt%W precursor powders calcined at 500 °C and 600 °C: (a) Cu-10 wt%W, 500 °C; (b) Cu-10 wt%W, 600 °C; (c) larger version of area A in Figure 12a; (d) larger version of area B in Figure 12b; (e) Cu-30 wt%W, 500 °C; (f) Cu-30 wt%W, 600 °C; (g) larger version of area C in Figure 12e; (h) larger version of area D in Figure 12e.

Precursor powders easily absorb water and agglomerate. When water is adsorbed on the surface of precursor powders, some crystalline water and volatile substances are removed first in the calcining process. When the calcination temperature is low, the calcined powders have less nucleation, and the growth trend of the powders is greater than the nucleation trend. At this time, the powders are transformed into bulk powders. When the calcination temperature is high, the nucleation number of the calcined powders increases and the nucleation trend is greater than the growth trend. At this time, the powders become fine and uniform. However, with the further increase in calcination temperature, the powders begin to agglomerate again due to the melting and bonding of the powder. During calcination,  $\text{Cu}_2(\text{OH})_3\text{NO}_3$  and  $\text{H}_2\text{WO}_4 \cdot \text{H}_2\text{O}$  in the precursor powders decompose

to form CuO and WO<sub>3</sub> (see reactions 6 and 7), and as calcination proceeds, CuO reacts with WO<sub>3</sub> to generate CuWO<sub>4</sub> (see reaction 8) [21,24].



### 3.3. Characterization of the Reduced Powders

XRD patterns of reduced powders are presented in Figure 13. Cu and W diffraction peaks are intense, and no spurious peaks exist, indicating that the powder composition is relatively pure after the two-stage reduction. With increasing tungsten content, the Cu diffraction peak gets weaker, and the W diffraction peak becomes higher, which is consistent with the design composition.

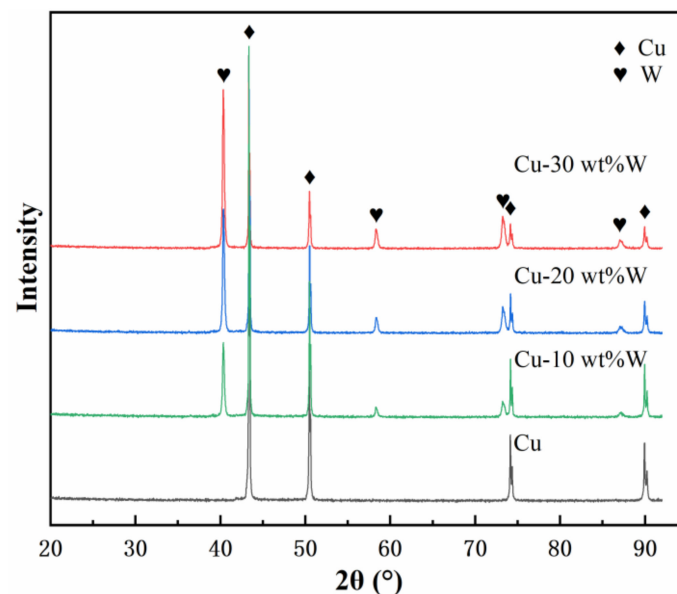


**Figure 13.** XRD patterns of reduced powders with various W contents.

SEM and BSE images of Cu-10 wt%W, Cu-20 wt%W, and Cu-30 wt%W reduced powders are shown in Figure 14. The atomic number of tungsten is larger than that of copper; the brighter color is W, and the darker color is Cu. The results are consistent with those in Figure 15. The formation of large particles and aggregates may be due to the hydrogen reduction process in which Cu is reduced first, and the two-stage hydrogen reduction time is too long, resulting in the melting of Cu particles and inter-particle bonding. The pure copper reduction powder maintains the morphology of the pure copper precursor powder calcined at 500 °C (see Figure 14a). The reason for the formation of the W-coated Cu structure is that volatile WO<sub>2</sub>(OH)<sub>2</sub> generated by tungsten oxides and water vapor in the reduction process is continuously deposited onto the Cu surface through CVT and reduced to W [30,31]. Nano-tungsten particles coated with copper particles gradually become denser and tend to grow from spherical particles to flake particles, with increasing tungsten content (Figure 14h–j). As marked by arrows 1–4 in Figure 14c,d, the copper particles coated with fewer tungsten particles have large particle sizes and serious melting phenomena between particles. In contrast, the copper particles coated with dense tungsten particles are less likely to melt and grow, indicating that this coating structure can inhibit the aggregation and growth of copper particles. However, the Cu-30 wt%W reduced powder, as shown in the C region in Figure 14d, shows an abnormal growth of some Cu particles, which may be related to the large CuO agglomerates in the calcined powder (Figure 12h). The elemental mapping of Cu-20 wt%W reduced powder demonstrates that Cu element and W element

distribution states are highly consistent, which is attributed to the solution molecular level doping and the chemical vapor transport of  $\text{WO}_2(\text{OH})_2$ .

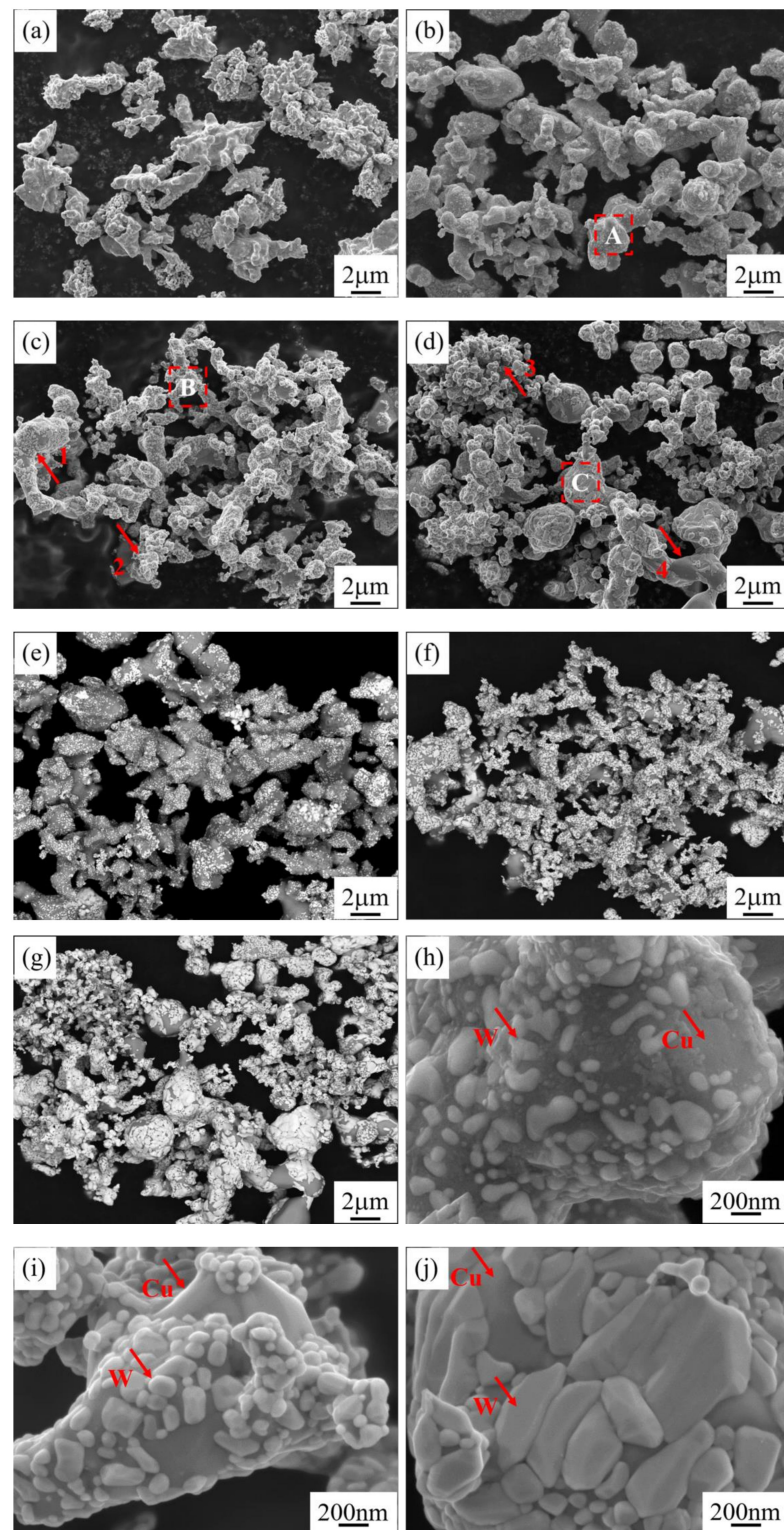


**Figure 14.** SEM and BSE images of Cu, Cu-10 wt%W, Cu-20 wt%W, and Cu-30 wt%W reduced powders: (a) SEM images of Cu; (b) SEM and (e) BSE images of Cu-10 wt%W; (c) SEM and (f) BSE images of Cu-20 wt%W; (d) SEM and (g) BSE images of Cu-30 wt%W; (h) enlarged view of area A of Figure 14b; (i) enlarged view of area B of Figure 14c; (j) enlarged view of area C of Figure 14d.

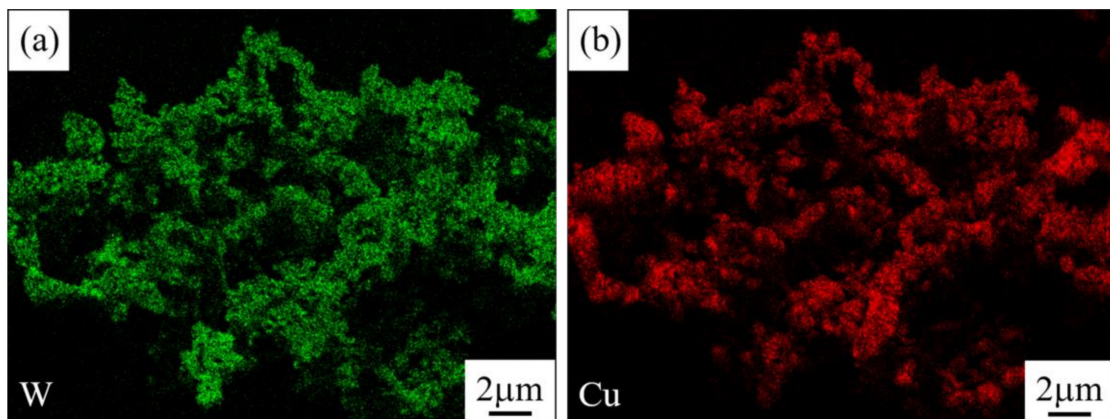


**Figure 15.** EDS distribution diagram of Figure 14e: (a) W; (b) Cu.

The TEM image of Cu-20 wt%W reduced powder is shown in Figure 16. The average size of the powder is about 200 nm, which exhibits a subspherical shape. It can be seen from the figure that the particle agglomeration phenomenon is serious, and there is an obvious sintering neck between the powder particles, which is consistent with the results in Figure 14c. Therefore, in order to obtain fine and well-dispersed Cu-W composite powder, it is necessary to reduce the second stage reduction temperature and reduce the reduction time.

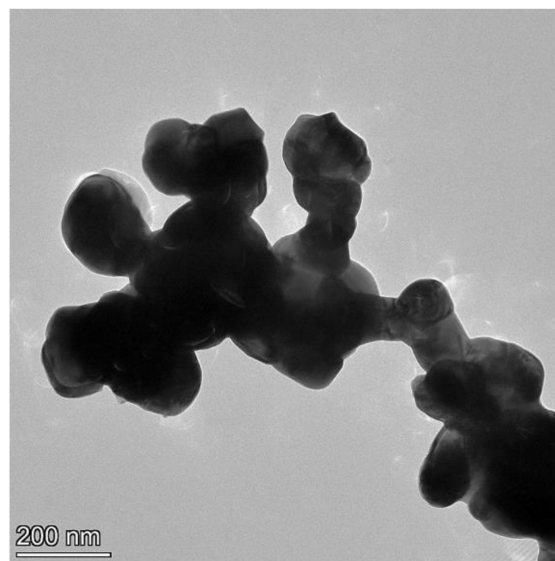
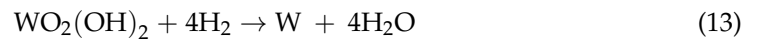
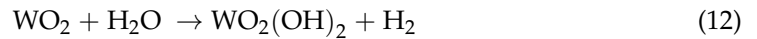
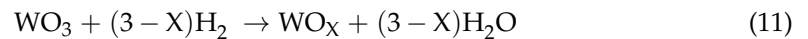
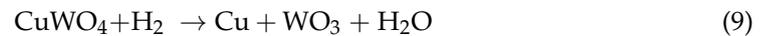


**Figure 16.** TEM image of Cu-20 wt%W reduced powder.

According to Li et al. [32], the calcined oxide powder phase evolution during the reduction process includes the reduction in the CuO phase at low temperatures, the reduction in the  $WO_3$  phase to a series of tungsten oxides ( $WO_{2.9}$  and  $WO_2$ ) at medium temperatures, and  $WO_2$  to W at high temperatures. Therefore, in the first reduction reaction, the reduction in Cu and partial reduction in  $WO_3$  to intermediates ( $WO_{2.9}$ ,  $WO_{2.72}$ , and  $WO_2$ ) mainly occur. Moreover, in the second reduction reaction, the reduction in W mainly occurs, including solid-phase diffusion (mainly oxygen migration) and chemical gas-phase migration [33]. As shown in Figure 17, the intermediate products react with water vapor to form volatile  $WO_2(OH)_2$ , which would migrate continuously to the Cu surface through CVT and be reduced to W, resulting in a Cu-W ultrafine composite powder with a W-coated Cu structure [34]. In this process, the first reduced copper dominantly acts

as heterogeneous nucleation while reducing the deposited nucleation of volatile  $\text{WO}_2(\text{OH})_2$ , resulting in a smaller tungsten particle size. The possible equation is as follows [32–34].



Curves of the frequency distribution and cumulative distribution of reduction powders with different W content are presented in Figure 18a–d. Each reduction powder size is approximately normally distributed.  $D_{10}$ ,  $D_{50}$ , and  $D_{75}$  values of reduction powders with different W content are given in Figure 18e. The particle sizes ( $D_{50}$ ) of Cu-10 wt%W, Cu-20 wt%W, and Cu-30 wt%W composite powders were 9.309  $\mu\text{m}$ , 8.440  $\mu\text{m}$ , and 6.290  $\mu\text{m}$ , which were reduced by 40.51%, 46.06%, and 59.80%, respectively, compared to the pure copper particle size of 15.648  $\mu\text{m}$ .

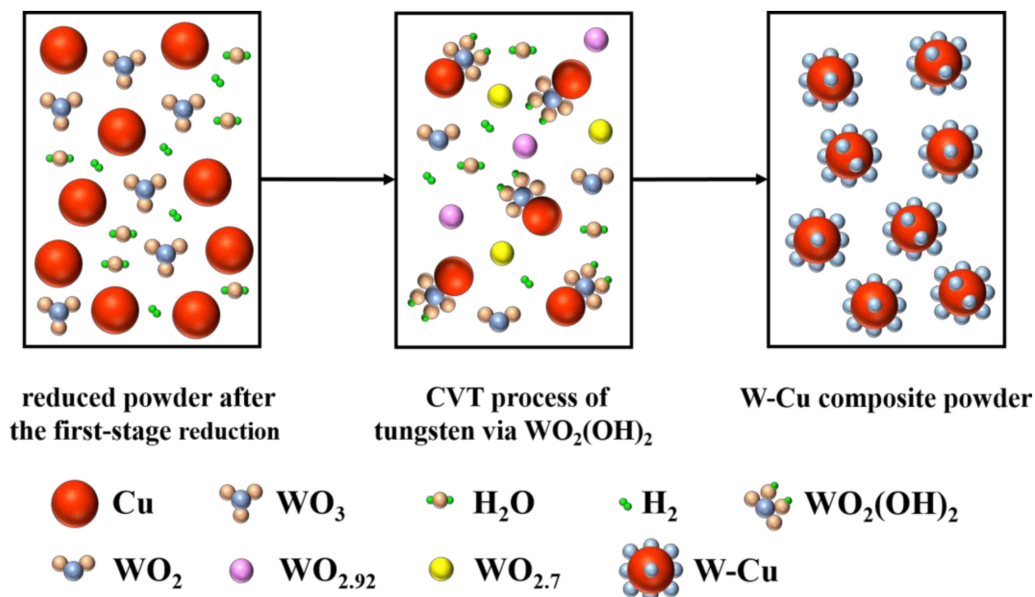


**Figure 17.** Phase evolution in the reduction in  $\text{WO}_3$ .

When the content of W is 30 wt%, the  $D_{50}$  of reduction powder reaches the lowest value, and the  $D_{10}$ ,  $D_{50}$ , and  $D_{75}$  values of reduced powder are the closest. Therefore, the growth of Cu particles can be effectively inhibited, and the uniformity of powder size can also be promoted by adding W particles [35]. The histogram of the particle size distribution of reduction powders with different W content is presented in Figure 18f; the difference between  $D(3, 2)$ ,  $D(4, 3)$ , and  $D_{50}$  of Cu-30 wt%W composite powder is the least. Therefore, Cu-30 wt%W composite powder has regular morphology and uniform size.

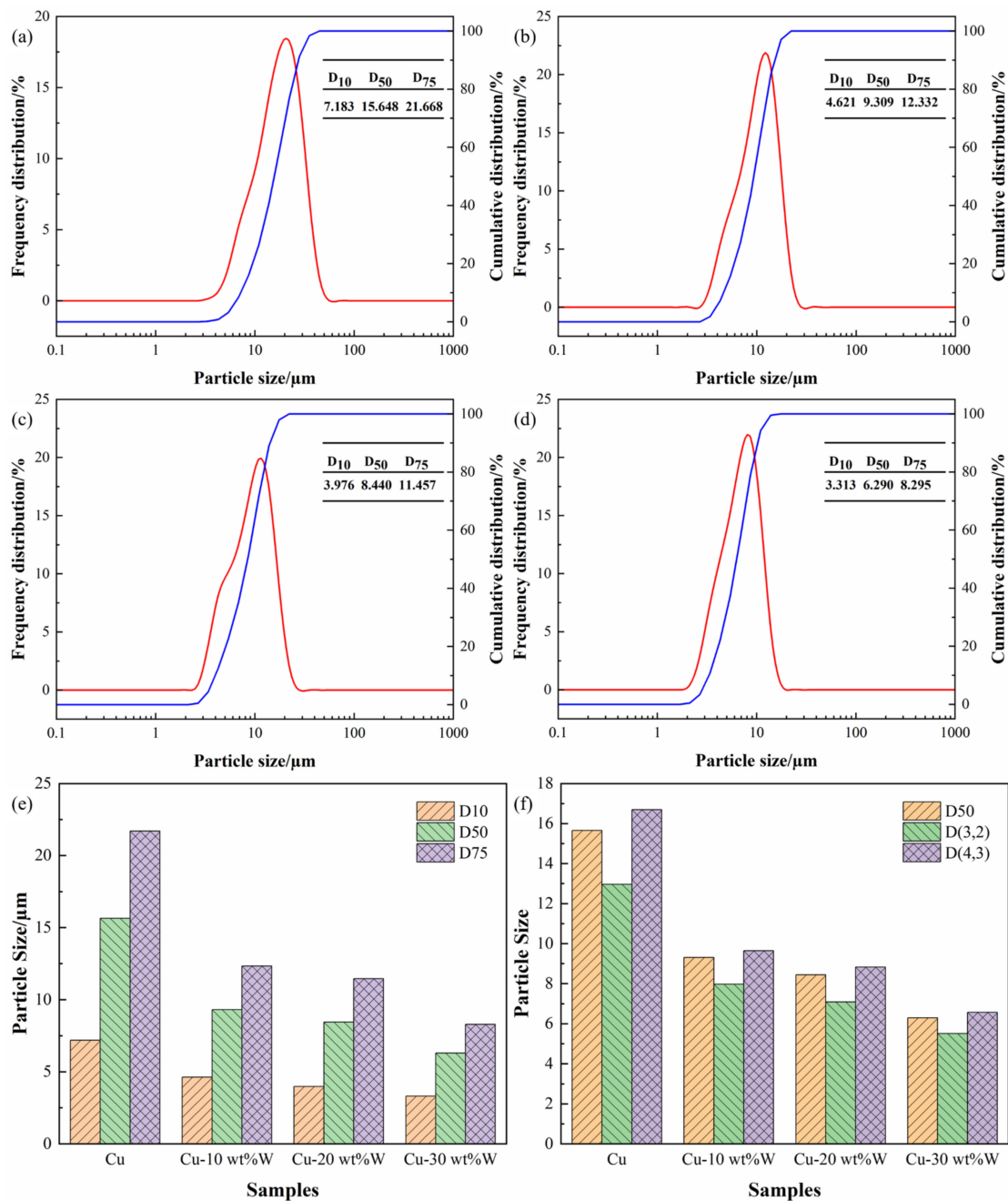


**Figure 18.** Particle size distribution: (a) Cu; (b) Cu-10 wt%W; (c) Cu-20 wt%W; (d) Cu-30 wt%W; (e) D10, D50, D75 values of the reduced powders (f) distribution histogram of the reduced powders.

#### 4. Conclusions

(1) XRD and FETEM measurements were carried out to confirm the presence of the  $\text{H}_2\text{WO}_4 \cdot \text{H}_2\text{O}$  in Cu-W precursor powder. Pure Cu precursor powder consisting of  $\text{Cu}_2(\text{OH})_3\text{NO}_3$  and Cu-W precursor powder consisting of  $\text{H}_2\text{WO}_4 \cdot \text{H}_2\text{O}$  and  $\text{Cu}_2(\text{OH})_3\text{NO}_3$  were prepared by the spray drying method. The Cu-W precursor powders are in the form of hollow spherical shells, and the distribution of Cu and W in the shell layer differs from that of the slate-like structure growing on the dependent surface. The slate-like structure growing on the dependent surface are dominantly  $\text{Cu}_2(\text{OH})_3\text{NO}_3$ .

(2) The calcination products of the pure copper precursor powder are pure CuO, while that of the Cu-W precursor powder are mainly CuO and  $\text{CuWO}_4$ . At different calcination temperatures, the calcined powders exhibit different phase compositions and

microstructures. The Cu-10 wt%W precursor powder calcined at 600 °C and Cu-20 wt%W precursor powder calcined at 500 °C both exhibited uniformly dispersed spherical CuWO<sub>4</sub> and flaky CuO, while Cu-30 wt%W calcined powders at 500 °C and 600 °C retain the hollow spherical shell of the precursor powders.

(3) After a two-stage hydrogen reduction, Cu-W composite powders with a nano-tungsten-coated copper particle structure was obtained. Tungsten nanoparticles deposited on the surface of copper particles can inhibit the aggregation and growth of copper particles. As the tungsten content increases, the inhibition becomes more intense, and the copper particles become finer. The particle sizes of Cu-30 wt%W composite powders are 6.290 μm, reduced by 59.80%, compared to the particle size of pure copper powder, 15.648 μm.

**Author Contributions:** Conceptualization, X.L. and S.W.; methodology, Q.W., X.L. and W.L.; investigation and data curation, Q.W. and W.L.; writing—original draft preparation, Q.W.; writing—review and editing, X.L., S.W., L.X. and Y.Z.; funding acquisition, X.L. All authors have read and agreed to the published version of the manuscript.

**Funding:** This research was funded by the Scientific and Technological Research Project of Henan Province, grant number 212102210453.

**Data Availability Statement:** Not applicable.

**Acknowledgments:** We wish to take this opportunity to thank the support of Henan University of Science and Technology 2021 Young Backbone Teacher Training Program, Provincial and Ministerial Collaborative Innovation Center of Non-ferrous Metal New Materials and Advanced Processing Technology, and Henan Key Laboratory of Non-ferrous Materials Science & Processing Technology. The authors acknowledge Wang Gong for his technical support and help with the spray dryer.

**Conflicts of Interest:** The authors declare no conflict of interest. The funders had no role in the design of the study, in the collection, analyses, or interpretation of data, in the writing of the manuscript, or in the decision to publish the results.

## References

1. Shu, D.; Li, X.; Yang, Q. Effect on Microstructure and Performance of B<sub>4</sub>C Content in B<sub>4</sub>C/Cu Composite. *Metals* **2021**, *11*, 1250. [[CrossRef](#)]
2. Li, X.Q.; Zhang, M.J.; Zhang, G.S.; Zhang, Q.; Wang, Q.; Wei, S.Z.; Xu, L.J.; Zhou, Y.C. Research on the hot deformation behavior of Cu-20 wt%W composite under different temperatures. *Mater. Sci. Eng. A Struct. Mater. Prop. Microstruct. Process.* **2022**, *830*, 9. [[CrossRef](#)]
3. Li, F.; Chen, Y.Y.; Chen, X.; Li, C.; Huang, Y. The Improvement of Bonding Strength of W/Cu Joints via Nano-Treatment of the W Surface. *Metals* **2021**, *11*, 10. [[CrossRef](#)]
4. Hao, Z.H.; Liu, J.X.; Cao, J.; Li, S.K.; Liu, X.W.; He, C.; Xue, X.Y. Enhanced Ductility of a W-30Cu Composite by Improving Microstructure Homogeneity. *Metals* **2019**, *9*, 11. [[CrossRef](#)]
5. Li, X.Q.; Zhang, M.J.; Zhang, G.S.; Wei, S.Z.; Xu, L.J.; Zhou, Y.C. Effect of spark plasma sintering temperature on structure and performance characteristics of Cu-20 wt%W composite. *J. Alloys Compd.* **2022**, *912*, 9. [[CrossRef](#)]
6. Hamidi, A.G.; Arabi, H.; Rastegari, S. A feasibility study of W-Cu composites production by high pressure compression of tungsten powder. *Int. J. Refract. Met. Hard Mater.* **2011**, *29*, 123–127. [[CrossRef](#)]
7. Liu, J.K.; Zhang, G.H.; Sun, G.D. Preparation of Ultrafine W-10 Wt Pct Cu Composite Powders and Their Corresponding Sintered Compacts. *Metall. Mater. Trans. A Phys. Metall. Mater. Sci.* **2019**, *50A*, 4827–4838. [[CrossRef](#)]
8. Wan, L.; Cheng, J.G.; Song, P.; Wang, Y.H.; Zhu, T. Synthesis and characterization of W-Cu nanopowders by a wet-chemical method. *Int. J. Refract. Met. Hard Mater.* **2011**, *29*, 429–434. [[CrossRef](#)]
9. Cheng, J.; Song, P.; Gong, Y.F.; Cai, Y.B.; Xia, Y.H. Fabrication and characterization of W-15Cu composite powders by a novel mechano-chemical process. *Mater. Sci. Eng. A Struct. Mater. Prop. Microstruct. Process.* **2008**, *488*, 453–457. [[CrossRef](#)]
10. Pillari, L.K.; Bakshi, S.R.; Chaudhuri, P.; Murty, B. Fabrication of W-Cu functionally graded composites using high energy ball milling and spark plasma sintering for plasma facing components. *Adv. Powder Technol.* **2020**, *31*, 3657–3666. [[CrossRef](#)]
11. Ma, D.Q.; Xie, J.P.; Li, J.W.; Liu, S.; Wang, F.M.; Zhang, H.J.; Wang, W.Y.; Wang, A.Q.; Sun, H.L. Synthesis and hydrogen reduction of nano-sized copper tungstate powders produced by a hydrothermal method. *Int. J. Refract. Met. Hard Mater.* **2014**, *46*, 152–158. [[CrossRef](#)]
12. Wang, X.R.; Wei, S.Z.; Xu, L.J.; Fang, F.; Li, J.W.; Pan, K.M.; Peng, B. Effect of sintering temperature on fine-grained Cu-W composites with high copper. *Mater. Charact.* **2019**, *153*, 121–127. [[CrossRef](#)]
13. Shi, X.L.; Yang, H.; Wang, S. Spark plasma sintering of W-15Cu alloy from ultrafine composite powder prepared by spray drying and calcining-continuous reduction technology. *Mater. Charact.* **2009**, *60*, 133–137. [[CrossRef](#)]

14. Li, C.G.; Zhou, Y.H.; Xie, Y.H.; Zhou, D.S.; Zhang, D.L. Effects of milling time and sintering temperature on structural evolution, densification behavior and properties of a W-20 wt.%Cu alloy. *J. Alloys Compd.* **2018**, *731*, 537–545. [[CrossRef](#)]
15. Qiu, W.T.; Pang, Y.; Xiao, Z.; Li, Z. Preparation of W-Cu alloy with high density and ultrafine grains by mechanical alloying and high pressure sintering. *Int. J. Refract. Met. Hard Mater.* **2016**, *61*, 91–97. [[CrossRef](#)]
16. Li, J.W.; Ma, D.Q.; Xie, J.P.; Fang, F.; Xu, L.J.; Wei, S.Z. A novel high density W-30Cu alloy prepared via hydrothermal synthesis-co-reduction and canned hot extrusion methods. *Metall. Res. Technol.* **2018**, *116*, 9. [[CrossRef](#)]
17. Chu, A.M.; Wang, Z.Q.; Rafi-ud-din; Dong, Y.H.; Guo, C.G.; Liu, W.H.; Xu, H.M.; Wang, L. Citric acid-assisted combustion-nitridation-denitridation synthesis of well-distributed W-Cu nanocomposite powders. *Int. J. Refract. Met. Hard Mater.* **2018**, *70*, 232–238. [[CrossRef](#)]
18. Hong, S.H.; Kim, B.K. Fabrication of W-20 wt %Cu composite nanopowder and sintered alloy with high thermal conductivity. *Mater. Lett.* **2003**, *57*, 2761–2767. [[CrossRef](#)]
19. Hong, S.H.; Kim, B.K.; Munir, Z.A. Synthesis and consolidation of nanostructured W-10-40 wt.% Cu powders. *Mater. Sci. Eng. A Struct. Mater. Prop. Microstruct. Process.* **2005**, *405*, 325–332. [[CrossRef](#)]
20. Fan, J.L.; Liu, T.; Zhu, S.; Han, Y. Synthesis of ultrafine/nanocrystalline W-(30-50)Cu composite powders and microstructure characteristics of the sintered alloys. *Int. J. Refract. Met. Hard Mater.* **2012**, *30*, 33–37. [[CrossRef](#)]
21. Wang, X.R.; Wei, S.Z.; Xu, L.J.; Li, J.W.; Li, X.Q.; Shan, K.N. Preparation of w-cu nano-composite powders with high copper content using a chemical co-deposition technique. *Adv. Powder Technol.* **2018**, *29*, 1323–1330. [[CrossRef](#)]
22. Yang, M.; Song, Z.; Lu, K. Synthesis of W-20%Cu nanocomposite powders. *Acta Metall. Sin.* **2004**, *40*, 639–642.
23. Yoon, E.S.; Lee, J.S.; Oh, S.T.; Kim, B.K. Microstructure and sintering behavior of W-Cu nanocomposite powder produced by thermo-chemical process. *Int. J. Refract. Met. Hard Mater.* **2002**, *20*, 201–206. [[CrossRef](#)]
24. Outokesh, M.; Hosseinpour, M.; Ahmadi, S.J.; Mousavand, T.; Sadjadi, S.; Soltanian, W. Hydrothermal Synthesis of CuO Nanoparticles: Study on Effects of Operational Conditions on Yield, Purity, and Size of the Nanoparticles. *J. Ind. Eng. Chem.* **2011**, *50*, 3540–3554. [[CrossRef](#)]
25. Khyzhun, O.Y.; Strunskus, T.; Cramm, S.; Solonin, Y.M. Electronic structure of CuWO<sub>4</sub>: XPS, XES and NEXAFS studies. *J. Alloys Compd.* **2005**, *389*, 14–20. [[CrossRef](#)]
26. Zhang, B.B.; Wang, L.; Zhang, Y.J.; Ding, Y.; Bi, Y.P. Ultrathin FeOOH Nanolayers with Abundant Oxygen Vacancies on BiVO<sub>4</sub> Photoanodes for Efficient Water Oxidation. *Angew. Chem. Int. Ed.* **2018**, *57*, 2248–2252. [[CrossRef](#)] [[PubMed](#)]
27. Chen, H.H.; Xu, Y.M. Photocatalytic organic degradation over W-rich and Cu-rich CuWO<sub>4</sub> under UV and visible light. *RSC Adv.* **2015**, *5*, 8108–8113. [[CrossRef](#)]
28. Zhu, J.W.; Li, D.; Chen, H.Q.; Yang, X.J.; Lu, L.; Wang, X. Highly dispersed CuO nanoparticles prepared by a novel quick-precipitation method. *Mater. Lett.* **2004**, *58*, 3324–3327. [[CrossRef](#)]
29. Zhang, Q.B.; Zhang, K.L.; Xu, D.G.; Yang, G.C.; Huang, H.; Nie, F.D.; Liu, C.M.; Yang, S.H. CuO nanostructures: Synthesis, characterization, growth mechanisms, fundamental properties, and applications. *Prog. Mater. Sci.* **2014**, *60*, 208–337. [[CrossRef](#)]
30. Ardestani, M.; Arabi, H.; Razavizadeh, H.; Rezaie, H.R.; Jankovic, B.; Mentus, S. An investigation about the activation energies of the reduction transitions of fine dispersed CuWO<sub>4-x</sub>/WO<sub>3-x</sub> oxide powders. *Int. J. Refract. Met. Hard Mater.* **2010**, *28*, 383–387. [[CrossRef](#)]
31. Wu, C.H. Preparation of ultrafine tungsten powders by in-situ hydrogen reduction of nano-needle violet tungsten oxide. *Int. J. Refract. Met. Hard Mater.* **2011**, *29*, 686–691. [[CrossRef](#)]
32. Li, Y.; Yu, S. Thermal-mechanical process in producing high dispersed tungsten-copper composite powder. *Int. J. Refract. Met. Hard Mater.* **2008**, *26*, 540–548. [[CrossRef](#)]
33. Ahmadi, E.; Malekzadeh, M.; Sadrnezhad, S.K. W-15 wt%Cu nano-composite produced by hydrogen-reduction/sintering of WO<sub>3</sub>-CuO nano-powder. *Int. J. Refract. Met. Hard Mater.* **2010**, *28*, 441–445. [[CrossRef](#)]
34. Hashempour, M.; Razavizadeh, H.; Rezaie, H.R.; Salehi, M.T. Thermochemical preparation of W-25%Cu nanocomposite powder through a CVT mechanism. *Mater. Charact.* **2009**, *60*, 1232–1240. [[CrossRef](#)]
35. Sun, T.L.; Xu, L.J.; Wei, S.Z.; Xiao, F.N.; Li, Z.; Fan, X.M.; Zhou, Y.C. Phase evolution of hydrothermal synthesis oxide-doped molybdenum powders. *Int. J. Refract. Met. Hard Mater.* **2020**, *86*, 12. [[CrossRef](#)]